SUPPLEMENTARY MATERIAL

CONTENTS

1. Supplementary Methods

1.1. Synthesis of diffusion couples

Diffusion couples were synthesized by hydrothermally growing rutile-saturated quartz over essentially Ti-free (<0.1 µg/g Ti), Al-bearing (~100 µg/g Al) synthetic quartz seeds. For this purpose, quartz bars measuring ~2x3x25 mm were cut out of a large, synthetic quartz crystal in such a manner that the crystallographic c-axis is perpendicular to two of the long sides of the bars. The surface of all four long sides was then finely polished using Al_2O_3 and SiC grinding papers and subsequently 1 µm and 1/4 µm diamond spray. The polished quartz bars were then loaded with crushed synthetic rutile (125-250 µm grain size) and distilled water into Pt capsules of 4.0 mm O.D, 3.7 mm I.D. and 35 mm length, such that the quartz bars were completely covered by the rutile grains and H_2O. In the two runs that were aimed to produce very Ti-rich overgrowths (SM01 and SM02), crushed SiO_2 glass (160-500 µm grain size) was admixed to the rutile (Fig. S1a).

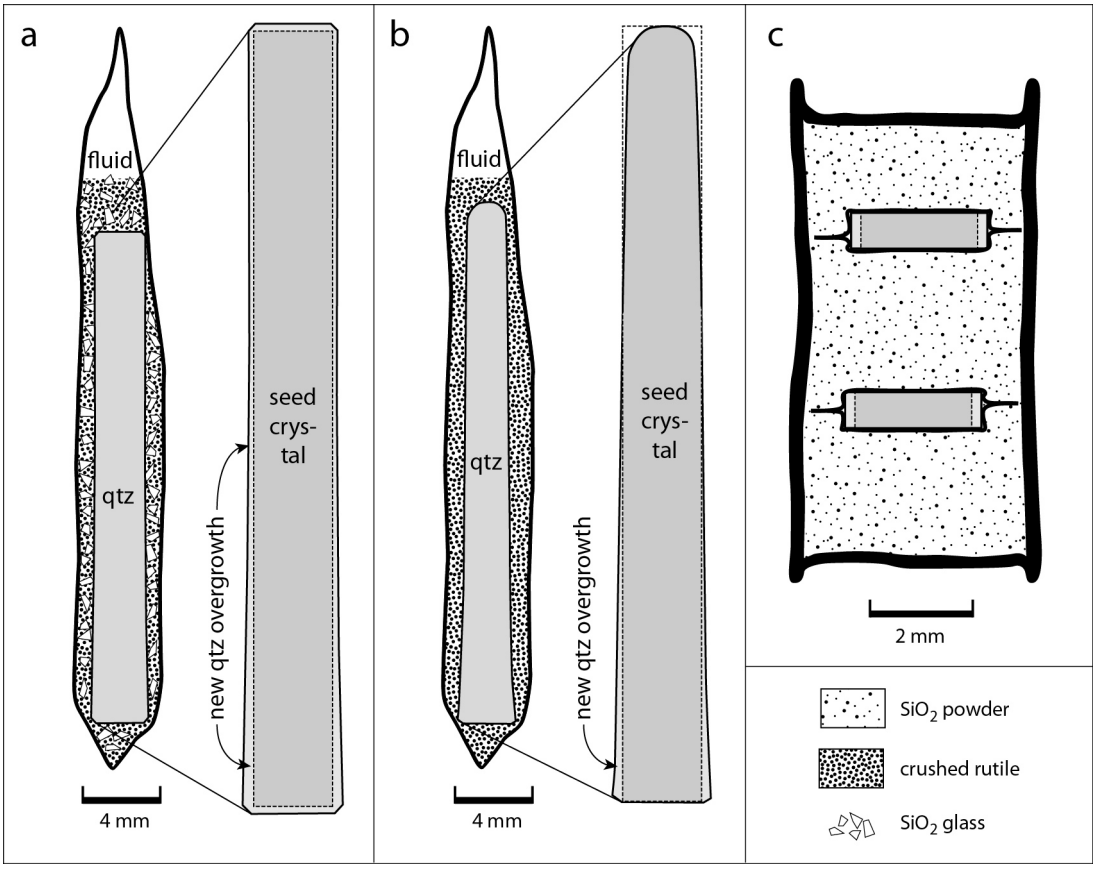

Figure S1: Schematic drawing of the utilized sample capsules.

These two capsules were run for 4-5 hours at 1,000 °C and 100 MPa in an Ar-pressurized TZM vessel. To avoid any quartz precipitation and gradual increase in Ti concentrations during the heating of the autoclaves the capsules were kept at the cold end of the autoclave until the final temperature was reached, and then they were brought within seconds with the help of an external magnet to the hot end of the autoclave. During the experiments, part of the crushed SiO_2 glass dissolved and re-precipitated on the ±Ti-free seed bars, and also part of the rutile recrystallized, resulting in a new quartz overgrowth containing 2,000-3,000 µg/g Ti and 70-100 µg/g Al. These Ti concentrations are

distinctly higher than the equilibrium value (855 µg/g) predicted by the model of Huang and Audétat (2012) because the quartz grew relatively rapidly in the presence of SiO_2 glass. Due to variations in growth rate the Ti and Al concentrations vary also within individual experiments. Part of the Ti in the Ti-rich starting material was thus hosted in crystal imperfections and may not have been able to diffuse properly if the annealing experiments were performed at the same P-T conditions. However, many annealing experiments were performed at 1 atm and 1,000-1,200 °C, at which conditions the predicted equilibrium Ti solubility is 2,800-5,600 µg/g. This means that during these experiments all Ti should have been fully dissolved in the crystal structure and, hence, to have diffused regularly. The same is true for the annealing experiment performed at 1,400 °C / 300 MPa, at which conditions the predicted Ti solubility is 2,500 µg/g, whereas in the experiments performed at 1,600 °C / 2 GPa the predicted solubility value (in this case poorly constrained) is 1,400 µg/g and thus below the 2,000-3,000 µg/g of the starting material. One capsule that did not contain any added SiO_2 glass was run for 166 hrs at 700 °C, 200 MPa in a conventional rapid-quench cold-seal pressure vessel in which H_2O was used as pressure medium (run SM03). In this case the upper parts of the quartz bar dissolved and re-precipitated very slowly onto the slightly cooler, lower part of the bar (Fig. S1b), forming a new quartz overgrowth that contained ~100 µg/g Ti (close to the equilibrium value of 851 µg/g) and ~370 µg/g Al. The Al in the new overgrowth stems mainly from the re-crystallization of rutile, which contained ~800 µg/g Al as impurity. All runs were terminated by slow (within ~10 seconds) in-situ quenching. The recovered quartz bars were then sectioned into 15-20 pieces perpendicular to the long axis of the bars using a low-speed diamond saw. The resulting slices were composed of a rectangular core of essentially Ti-free quartz, which on four sides are surrounded by Ti-enriched quartz (supplementary Figs. S2-S3). Both quartz generations extinguished fully and simultaneously under crossed nicols in the petrographic microscope, suggesting undisturbed epitaxial growth. Furthermore, CL, TEM and HIM-SIMS maps of these starting materials revealed perfect step functions of the Ti concentrations at the core-rim contacts within the spatial resolution of each technique (~0.2 µm in CL; ~0.07 µm in HIM-SIMS; ~0.04 µm in TEM-EDXS; see below).

1.2. Annealing experiments

Individual slices of the synthesized diffusion couples were annealed either in 1 atm gas mixing furnaces or at 0.3-2.0 GPa in piston cylinder presses. Experiments at 1 atm were successful only at ≤1,300 °C because at higher temperatures the quartz transformed to tridymite within less than three days. In contrast, high-pressure experiments performed with the Ti-rich starting material were successful only at ≥1,400 °C because at lower temperatures the quartz became Ti-oversaturated and exsolved rutile crystals. The high-pressure experiments performed with the Ti-poor starting material were not affected by this problem. The experiments in the gas mixing furnaces lasted for 3-85 days and were conducted in air. The temperature in these furnaces was measured by type S ($Pt_{100}/Pt_{90}Rh_{10}$) thermocouples and should be accurate within 5-10 °C. For the piston cylinder experiments slices of the diffusion couples were welded into 0.1 mm Pt foils and then filled with SiO_2 powder into PtRh capsules of 5.0 mm O.D., 4.3 mm I.D. and 10 mm length, which subsequently were welded shut (Fig. S1c). The experiments were conducted in end-loaded piston cylinder presses using mostly 1/2" talc-pyrex-crushable Al_2O_3

assemblies with a tapered graphite furnace. Temperature in these runs was measured by type D ($W_{97}Re_{03}/W_{75}Re_{25}$) thermocouples and is known to only about ±50 °C due to temperature gradients arising from irregular deformation of the graphite furnace during pressurization. A friction correction of 20% was applied based on calibrations of the quartz-coesite transition and the albite to jadeite+quartz transition. For one experiment a MgO-NaCl assembly with stepped graphite heater was used. The uncertainty in temperature in this assembly is about ±30 °C and the friction correction is much lower (ca. 100 MPa, independent of the P-T conditions). The piston cylinder experiments were conducted at 0.3-2.0 GPa, 1,100-1,600 °C and durations of 2-34 days. The runs were terminated by lowering the temperature within ca. 1 minute and lowering the pressure within ca. 30 minutes. The recovered quartz slices were embedded with the surrounding Pt-foils in epoxy and then polished about 1/3 down to remove any diffusion profiles on their surface. The samples were then polished with 1/4 µm diamond on Al foil to ensure a flat sample surface. An overview of the conducted experiments is given in supplementary Table S1.

1.3. Cathodoluminescence imaging

The sample mounts were coated with 12-13 nm carbon prior to imaging. Polychromatic cathodoluminescence (CL) images were produced with a Zeiss Gemini 1530 field emission gun (FEG) scanning electron microscope equipped with an ellipsoidal mirror and a photomultiplier detector that detects all light in the visible range. The images were taken at a resolution of 1024 × 768 pixels and a scan rate of 5-10 min/image, often scanning only a small part of the image (i.e., the immediate vicinity of the contact between low-Ti and high-Ti quartz) in order to save time. To achieve a high spatial resolution a low acceleration voltage was used (see e.g., the discussion in Gualda and Sutton, 2016). However, with decreasing voltage also the sensitivity decreases. In our instrument the optimal compromise between high spatial resolution and sufficient sensitivity was found at 7 kV and using an aperture of 120, which corresponds to ca. 5 nA sample current. The working distance was kept at around 14 mm. In the Ti-rich diffusion couples (2,000-3,000 µg/g Ti in the new quartz overgrowth) the image contrast was set such that either the low-luminescent side was not totally black or the high-luminescent side was not totally white; in the Ti-poor diffusion couples (~100 µg/g Ti) and in the natural quartz samples the contrast was set such that neither side was totally black or totally white. Using these settings a spatial resolution corresponding to a full width at half maximum (FWHM) of 0.18-0.19 µm was achieved in slow scans of highly magnified core-rim contacts and healed cracks in the Ti-rich starting material, and a FWHM of 0.42 µm in fast scans of the less Ti-rich starting material at slightly lower magnification.
The synthetic Ti-rich diffusion couples and the magmatic quartz phenocryst from the Bandelier Tuff displayed consistently higher luminescence in the Ti-rich overgrowth than in the Ti-poor core, independent of magnification and scan speed (supplementary Figs. S4-S5). In contrast, the synthetic Ti-poor diffusion couples showed an unusual CL behavior at high magnifications: whereas at fast scan rates (~2 s/image) the luminescence intensity was higher on the Ti- and Al-rich side than on the Ti- and Al-poor side (as usual), the profiles inverted at slow scan rates (5-10 min/image) at high magnifications (supplementary Fig. S6). Furthermore, in some of these samples a pronounced luminescence low developed at the boundary between Ti-poor and Ti-rich quartz,

resulting in grayscale profiles that do not resemble diffusion profiles (supplementary Fig. S7). The same effects were observed in a natural, low-temperature hydrothermal quartz sample (supplementary Fig. S8). Götze (2009) reports that in hydrothermally-grown quartz crystals (both natural and synthetic ones) the CL emission at 390 nm wavelength decreases rapidly during electron bombardment, and that this luminescence centre is related to Al. It is thus possible that some of the luminescence profiles observed in our synthetic, Ti-poor diffusion couples do not mirror the Ti distribution, but rather the distribution of Al or some other luminescence centres. If so, then the latter applies more likely for the inverted profiles because in natural, high-temperature (> 400 °C) quartz crystals examined at relatively low magnification the luminescence intensity generally correlates with Ti concentration (Rusk, 2012). Independent of which elements or defects caused the luminescence in these samples, if both the normal profiles obtained during fast scanning and the inverted profiles obtained during slow scanning are not longer than e.g., 1.0 µm, then none of the luminescence-producing elements should have diffused over longer distance. For this reason we always quantified the longer diffusion profile obtained at fast scanning rates (e.g., supplementary Fig. S6), and the diffusion coefficients derived from these synthetic low-Ti diffusion couples should thus represent maxima.

1.4. TEM mapping

Thin foils measuring ca. 20x10x2 µm were cut out across the diffusion couple interfaces with the help of a focused ion beam instrument (FIB; FEI Scios DualBeam) using a Ga^+ ion beam at 30 kV and 5-20 nA. The foils were subsequently thinned to a thickness of 100-200 nm using a low current of 100-300 pA. Before loading the foils into the TEM instrument they were plasma-cleaned in order to remove surface hydrocarbon contamination. Energy-dispersive X-ray spectroscopy (EDXS) maps of the samples were performed with a field emission scanning transmission electron microscope (FEI, Titan G2 80-200 S/TEM) equipped with an energy-dispersive X-ray spectrometer system (4 silicon drift detectors, Bruker Quantax). The maps were taken at a resolution of 4-10 nm per pixel and a dwell time of 16 µsec using a sub-nanometer-sized electron beam with less than 0.07 nA probe current at 200 kV acceleration voltage. To accumulate statistically enough Ti counts in the quantitative EDXS maps, the total acquisition time was 30 to 120 minutes. During signal acquisition, an image drift correction function was activated to prevent artificial broadening of the diffusion profiles.

In addition to the EDXS maps, high-angle annular dark-field (HDAAD), bright-field (BF), annular bright-field (ABF) and dark-field (DF) images were acquired to determine the lattice orientation of the quartz and to check for defect structures and the presence of TiO_2 inclusions. In all cases the new Ti-bearing quartz grew perfectly epitaxially onto the Ti-free substrate without the formation of abundant defects at the contact, and the quartz was free of TiO_2 inclusions except in the high-pressure runs performed with the Ti-rich starting material at <1400 °C, which exsolved small, stubby to needle-shaped rutile crystals (supplementary Fig. S10) because the Ti-solubility in the quartz was exceeded.

1.5. HIM-SIMS mapping

A helium ion microscope (HIM) coupled with a secondary ion mass spectrometer (SIMS) (Wirtz et al., 2016; Dowsett and Wirtz, 2017) was used to evaluate the distribution of Ti in two Ti-rich starting materials and in one Ti-rich sample after annealing. The HIM

exhibits substantially higher resolution (~0.3 nm with a He^+ ion beam; ~2 nm with a Ne^+ ion beam) and surface sensitivity than modern Scanning Electron Microscopes (SEM) or Focused Ion Beam (FIB) systems. To provide analytic information, a mass spectrometer was specifically designed and developed at LIST for the HIM Orion Nanofab microscope (Zeiss, Peabody, USA). In principle, this setup is capable of producing elemental SIMS maps with a lateral resolution about 20 nm (Dowsett and Wirtz, 2017; Kim et al., 2019). In this study, the HIM-SIMS system was optimized for the collection of the secondary ions generated by a Neon primary ion bombardment (Ne^+, 20 keV, 3 pA), which were transmitted to the high-performance double focusing magnetic sector mass spectrometer and finally detected in a multi-collector system (4 Channel Electron Multipliers) (Usiobo et al., 2020). For the analysis of the quartz samples, the instrument was tuned for the detection of titanium (^{48}Ti, m= 47.9479 amu) and silicon (^{28}Si, m=27.9769 amu) isotopes in a matrix of 512x512 pixels with a counting time of 5 ms/pixel.

1.6. BSE imaging

In sanidine crystals with relatively high Ba concentrations and more or less constant orthoclase component the backscattered electron (BSE) intensity is a function of Ba content (Ginibre et al., 2014). The BSE images were acquired on a JEOL JXA-8200 microprobe using 15 kV, 20 nA, a focused beam, a scan rate of 31 seconds per image and an image resolution of 1280x1024 pixels. In some sanidine phenocrysts a narrow zone of intermediate gray shade was observed at the contact between Ba-poor core and Ba-rich overgrowth, suggesting a real growth zonation (i.e., an imperfect step function) prior to annealing. For this reason only the shortest Ba diffusion profiles were considered as representative.

1.7. LA-ICP-MS analysis

LA-ICP-MS analyses of quartz, sanidine and melt inclusions were performed using a 193 nm ArF Laser (GeolasPro; Coherent, USA) attached to a quadrupole ICP-MS (Elan DRC-e; Perkin Elmer, Canada). Diffusion profiles in sanidine were measured using a rectangular laser beam of ~5x50 µm size whose long axis was oriented parallel to the growth zoning. The laser fluence at the sample surface was about 10 J/cm^2 and the laser repetition rate was 7 Hz. For the analysis of quartz and quartz-hosted melt inclusions round laser pits, a fluence of about 15 J/cm^2 and a repetition rate of 10 Hz was used. All measurements were performed in a rhombic sample chamber with an internal volume of ~8 cm^3, which was flushed with He at a rate of 0.4 l/min, to which 5 ml/min H_2 was admixed on the way to the ICP-MS. The ICP-MS system was tuned to a ThO rate of 0.07-0.10% and a rate of doubly-charged Ca ions of 0.14-0.20% according to measurements on NIST SRM 610 glass. Analyzed isotopes comprise ^{7}Li, ^{11}B, ^{23}Na, ^{25}Mg, ^{29}Si, ^{30}Si, ^{39}K, ^{43}Ca, ^{49}Ti, ^{55}Mn, ^{57}Fe, ^{85}Rb, ^{88}Sr, ^{89}Y, ^{90}Zr, ^{93}Nb, ^{98}Mo, ^{118}Sn, ^{133}Cs, ^{137}Ba, ^{140}Ce, ^{187}W, ^{208}Pb, ^{209}Bi, ^{232}Th and ^{238}U, using dwell times of 10-40 ms per isotope. External standardization was primarily based on NIST SRM610, except for the major and minor elements in the melt inclusions, which were standardized based on a well-characterized natural obsidian glass. Internal standardization of the melt inclusions (which were all glassy) was based on the Al_2O_3 content of a few large, exposed melt inclusions, which could be analyzed without co-ablation of quartz host. For quartz a SiO_2 concentration of 100 wt% was used as internal standard, and for sanidine analyses the sum of all major and

minor elements was normalized to 100 wt%. An overview of the diffusion coefficients obtained from the Shaggy Peak Rhyolite is provided in supplementary Table S2.

1.8. Thermobarometry

The P-T formation conditions of the quartz phenocrysts of the Shaggy Peak Rhyolite were reconstructed using the approach described in Audétat (2003). In this approach, the composition of melt inclusions (specifically their content of Zr and all major plus minor elements including TiO_2) is used to constrain temperature via zircon saturation thermometry (Watson and Harrison, 1983) plus the activity of TiO_2 based on the TiO_2 solubility model of Kularatne and Audétat (2014). The Ti content of the host quartz is then used in conjunction with the TiO_2 activity and zircon saturation temperatures to calculate the entrapment pressure based on the TitaniQ model of Huang and Audétat (2012). The presence of zircon inclusions in quartz and feldspar phenocrysts of the Shaggy Peak Rhyolite confirms that the magma was zircon saturated. The compositions of eight melt inclusion – quartz pairs and the corresponding P-T conditions are summarized in supplementary Table S3. The results suggest that the Ti-rich rims of the quartz phenocrysts formed after a magma mixing event that occurred at ~730 °C and 300-400 MPa pressure. If the pressure were calculated based on the TitaniQ model of Thomas et al. (2010) instead of the one of Huang and Audétat (2012) they would turn out at 1.0-1.1 GPa. The dark-luminescent, Ti-poor cores of the quartz phenocryst cores grew at ~690 °C from a melt that contained 4-30 µg/g Ba, 3-14 µg/g Sr, and 15-18 µg/g Cs, and the high-luminescent, Ti-rich rims grew at ~730 °C from a melt that contained 500-600 µg/g Ba, 80-90 µg/g Sr, and 4-6 µg/g Cs.

1.9. Determination of diffusion coefficients using PACE

All diffusion profiles that were extracted with the help of ImageJ from the maps showed relatively flat plateaus on both sides and thus were fitted in PACE with the equation:

$$C(x,t) = C_2 + (C_1 - C_2) \times \frac{1}{2} \times erfc\left(\frac{x - X}{2\sqrt{Dt}}\right)$$

in which C (x,t) denotes the concentration at position x and time t, X the inflection point of the profile and D the diffusion coefficient (m^2s^{-1}).

Signal deconvolution was performed using the FWHM distance determined at the contact between Ti-poor and Ti-rich quartz in the starting materials using the corresponding analytical technique, and a Gaussian interaction volume was assumed in all cases. In the case of the natural quartz phenocryst the diffusion coefficient was calculated by subtracting the initial Dt value from the final one and then dividing through time.

2. Supplementary Figures

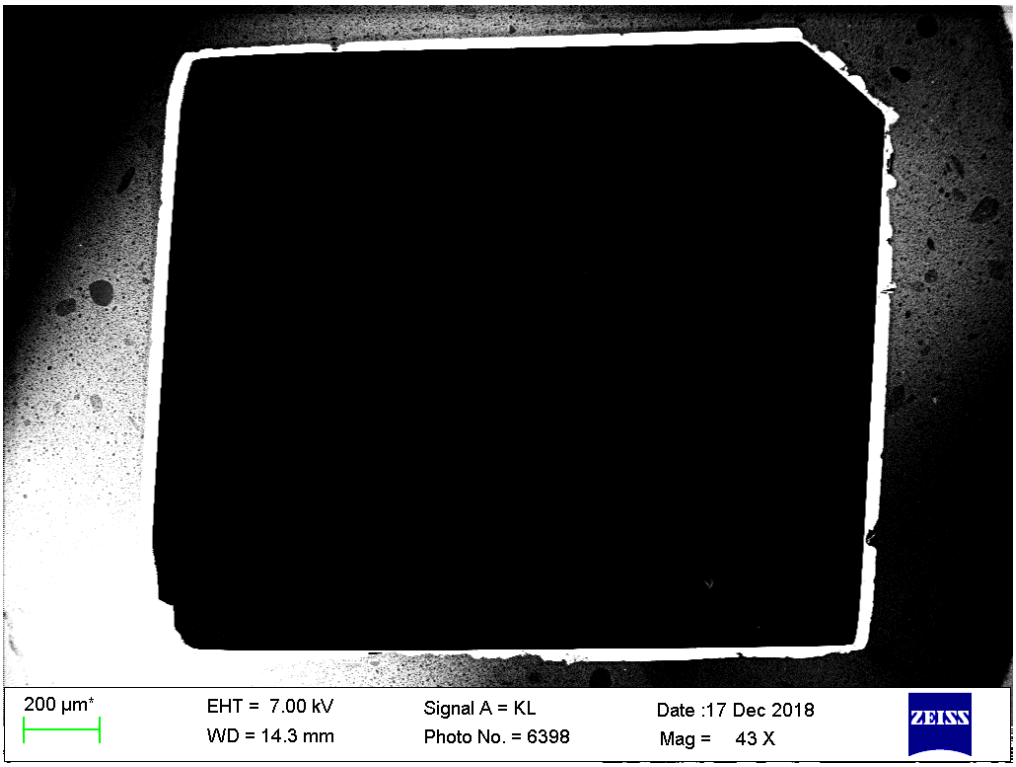

Supplementary Figure S2. Cathodoluminescence image of a slice of the Ti-rich diffusion couple starting material SM02, which features a black, ±Ti-free quartz core over which a thin quartz layer containing 3,000 µg/g Ti (showing up white in the image) was grown hydrothermally.

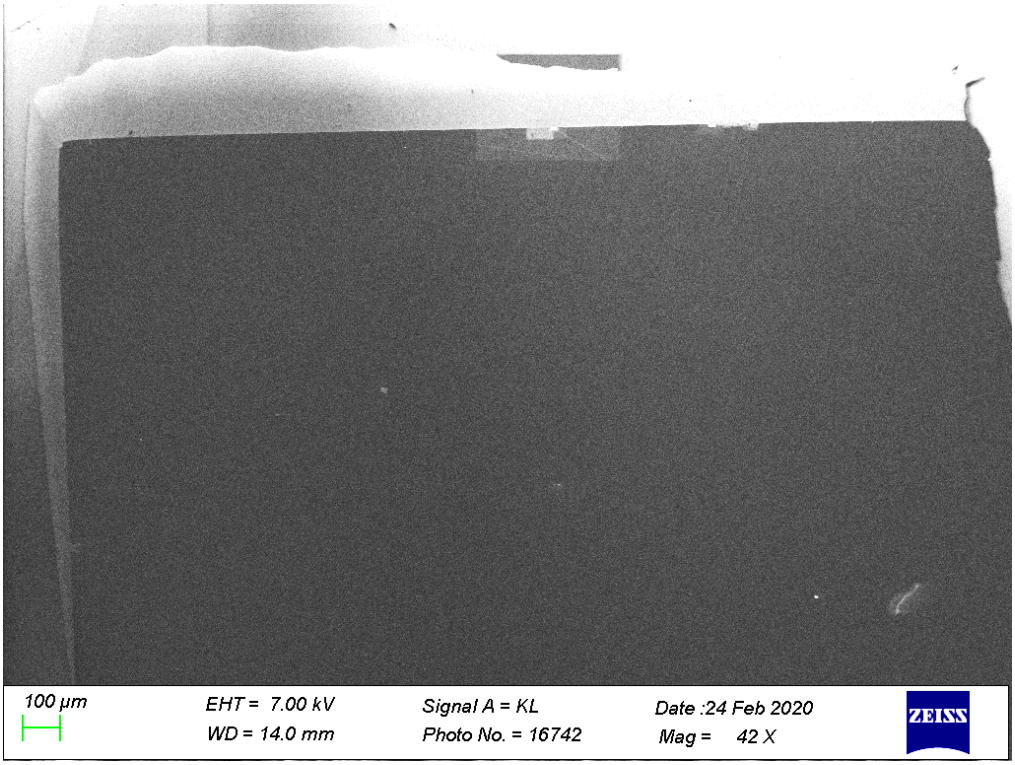

Supplementary Figure S2. CL image of a slice of the starting Ti-poor diffusion couple starting material SM03, which contains ~100 µg/g Ti in the new quartz overgrowth. The bright rectangles at the boundary between old and new quartz are electron beam damages from previous images taken at higher magnification.

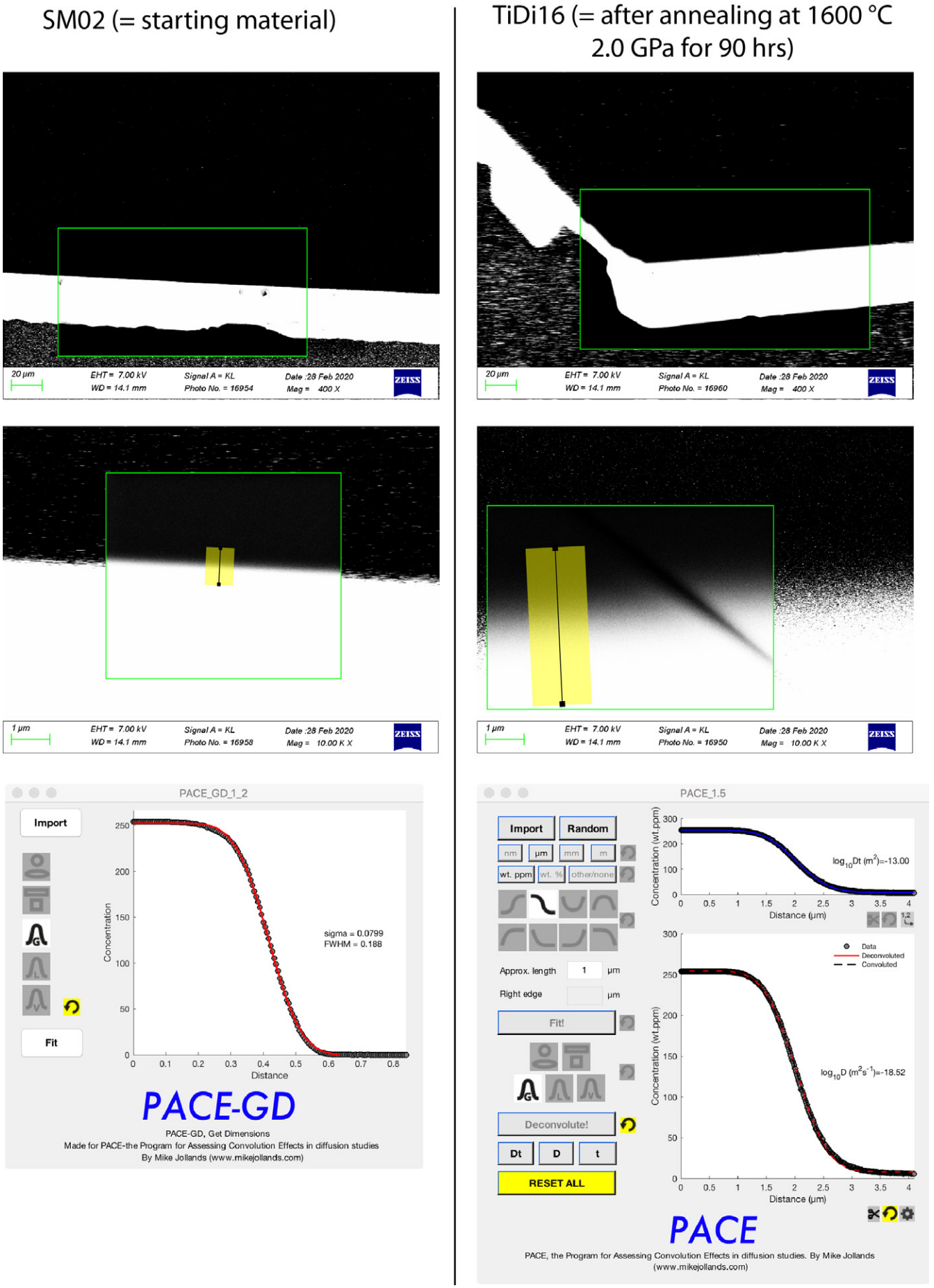

Supplementary Figure S4. CL images, ImageJ profiles (yellow, semitransparent areas) and PACE fits of a synthetic, Ti-rich diffusion couple before and after annealing at 1,600 °C and 2.0 GPa for 90 hours.

The untreated half of the quartz phenocryst:

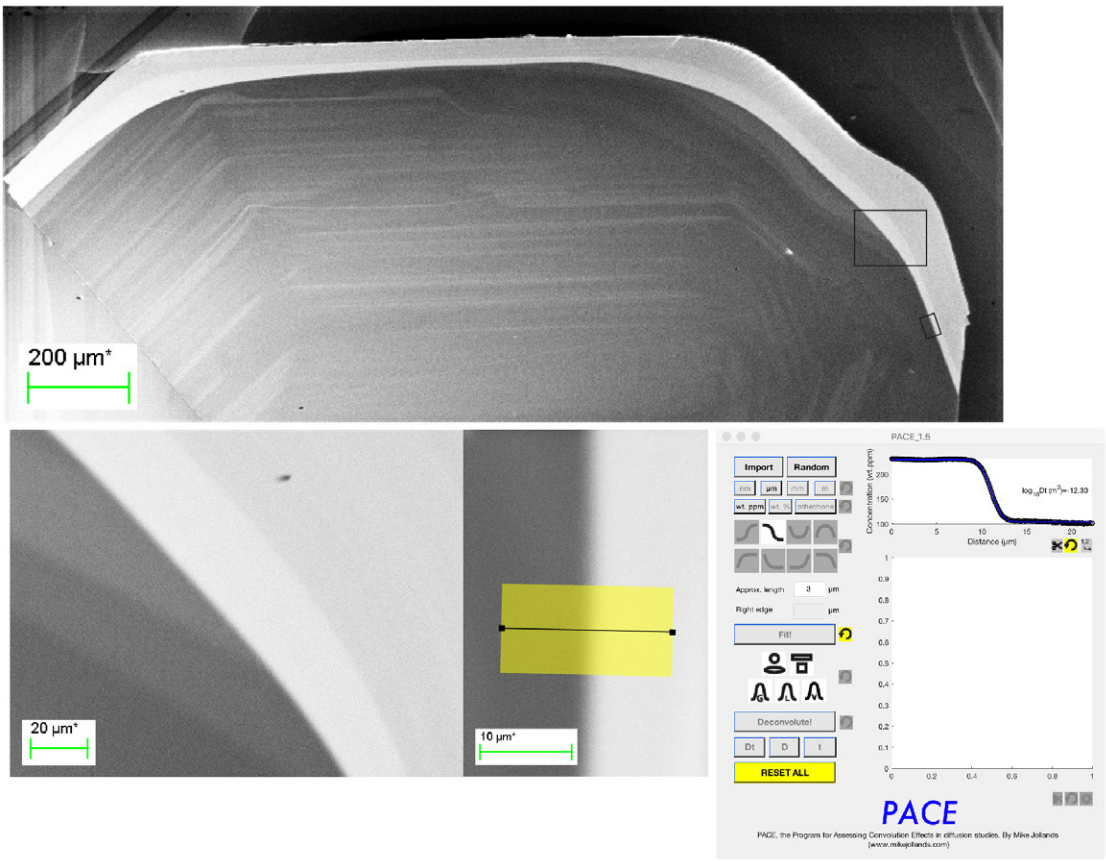

The other half of the same phenocryst after 75 hrs at 1600 °C / 2.0 GPa:

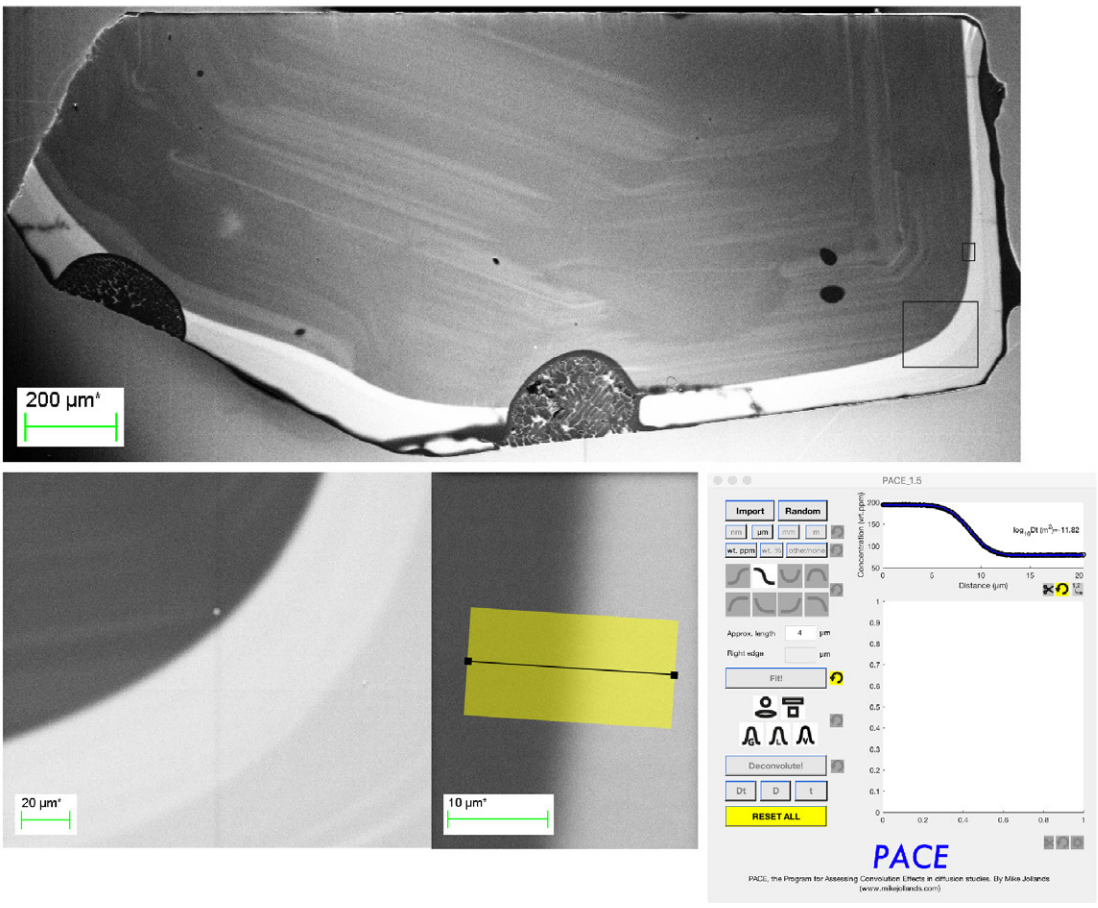

Supplementary Figure S5. CL images, ImageJ profiles (yellow areas) and PACE fits of two halves of the same quartz phenocryst from the Upper Bandelier Tuff, New Mexico, USA.

SM03 (= starting material)

TiDi45 (= after annealing at 1200 °C 1 tm for 473 hrs)

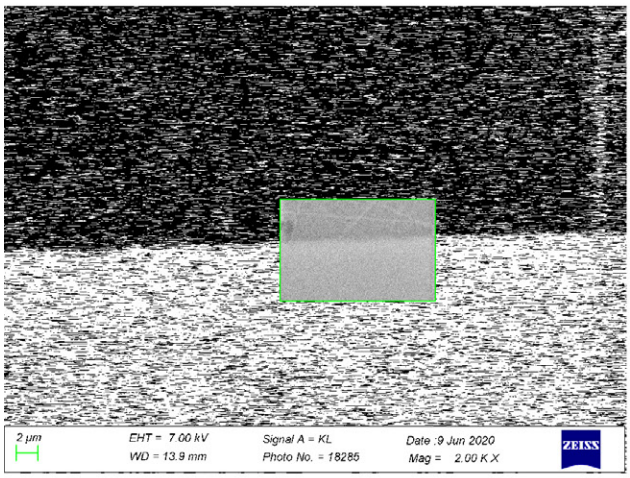

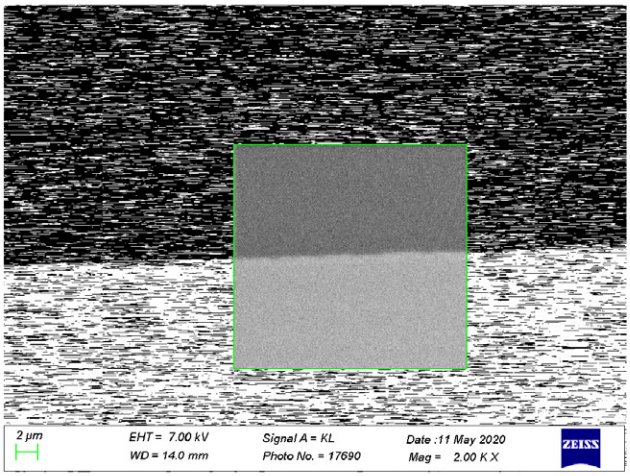

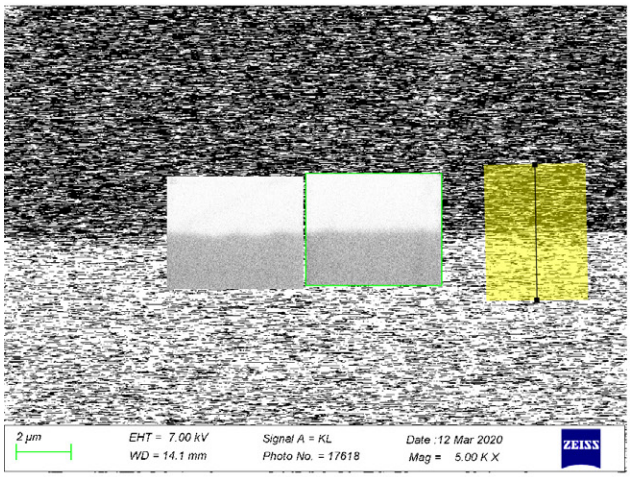

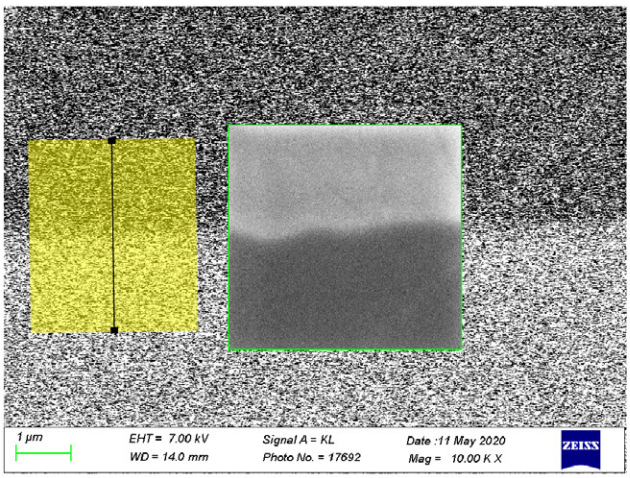

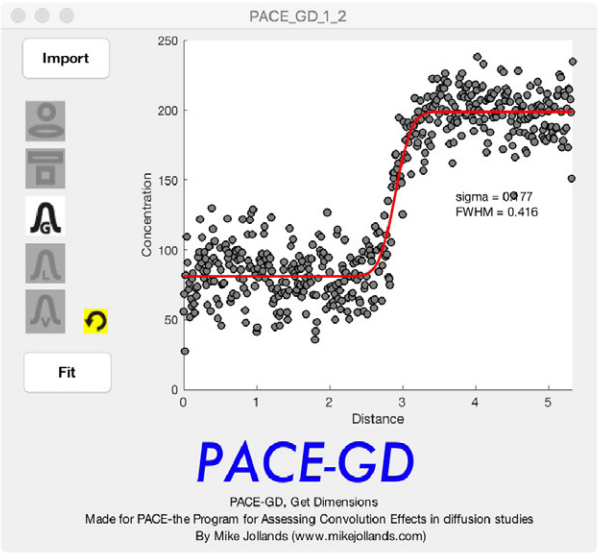

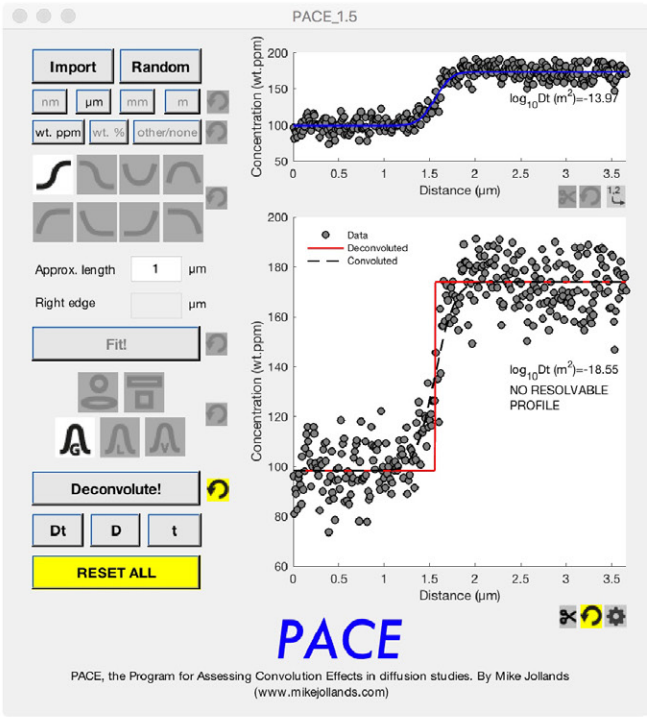

Supplementary Figure S6. CL images, ImageJ profiles (yellow areas) and PACE fits of a synthetic low-Ti diffusion couple before and after annealing at 1,200 °C and 1 atm. The coarse-grained parts of the images were scanned at fast rates (ca. 2 s / image), whereas the highly resolved insets were scanned at slow rates (ca. 2 minutes per inset). Notice the inverse CL distribution in the insets at very high magnification.

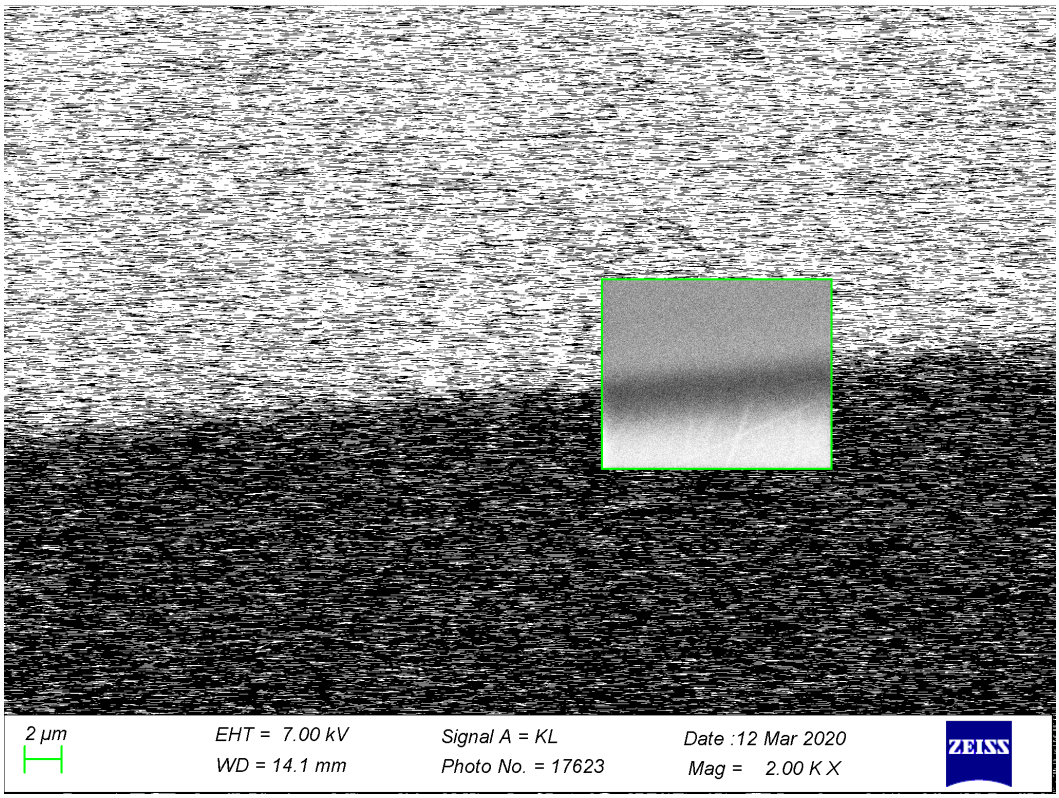

Supplementary Figure S7. Cathodoluminescence image of sample TiDi41, which showed the most pronounced luminescence low at the contact between Ti-bearing and Ti-poor quartz at slow scan rates.

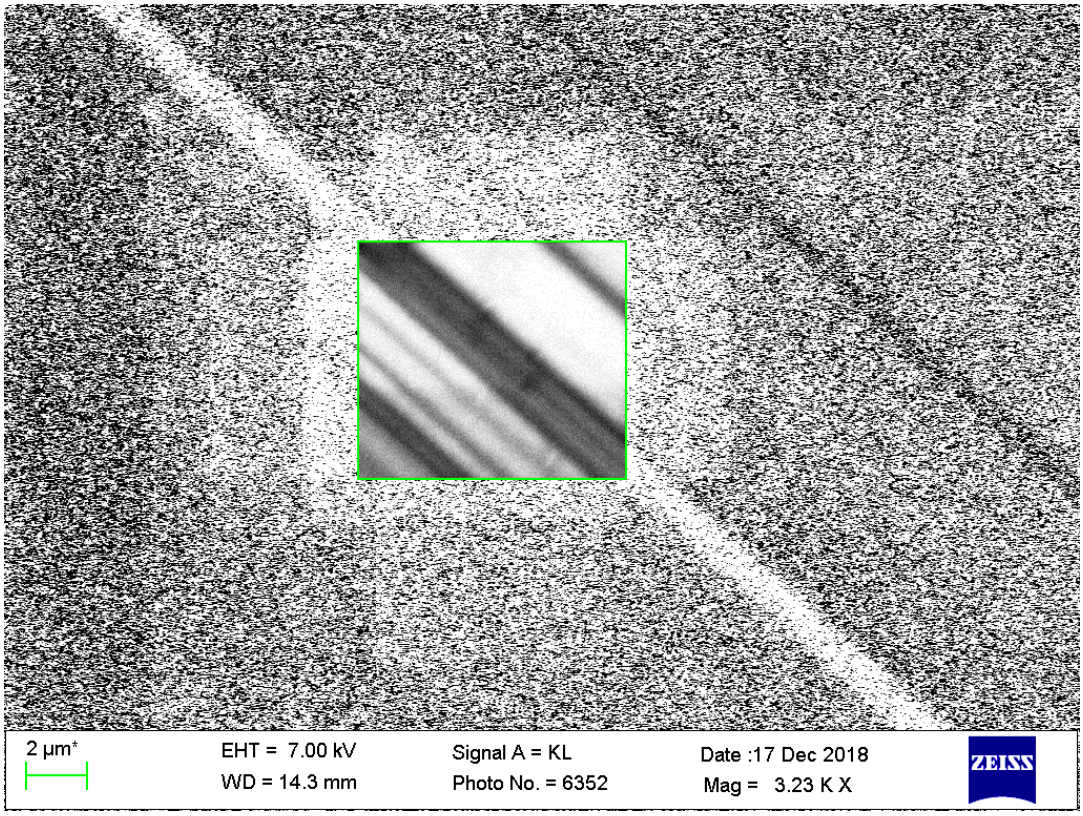

Supplementary Figure S8. Cathodoluminescence image of a natural, low-temperature (<400 °C) hydrothermal quartz from the Cañada Pinabete Pluton, New Mexico (USA). Similar to the synthetic low-Ti diffusion couple, the luminescence intensities got inversed during slow scanning at high magnifications and dark band developed at the contact between individual layers.

SM02 (= starting material)

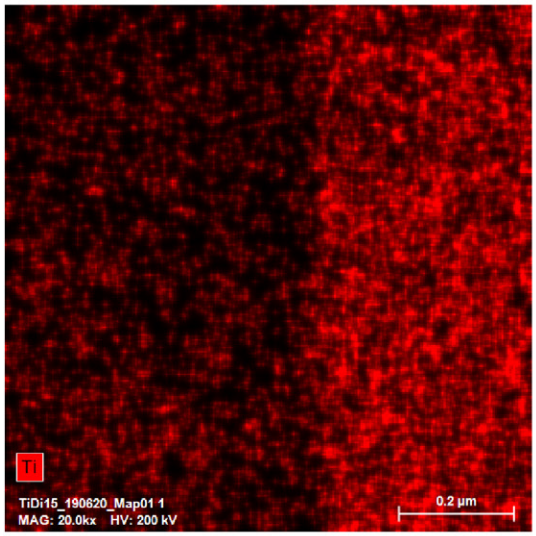

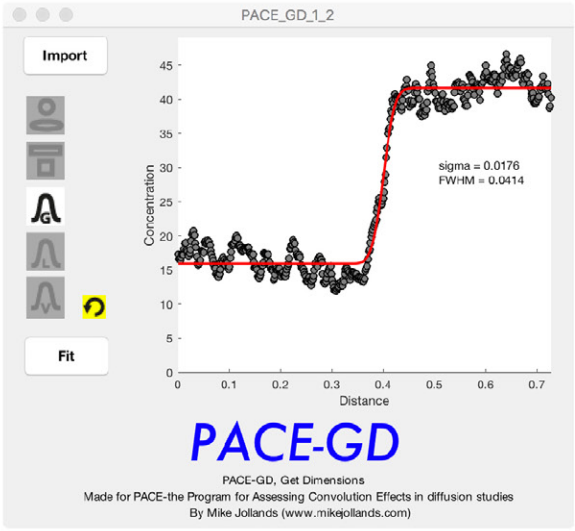

TiDi22 (= after annealing at 1000 °C, 2.0 GPa for 2033 hrs)

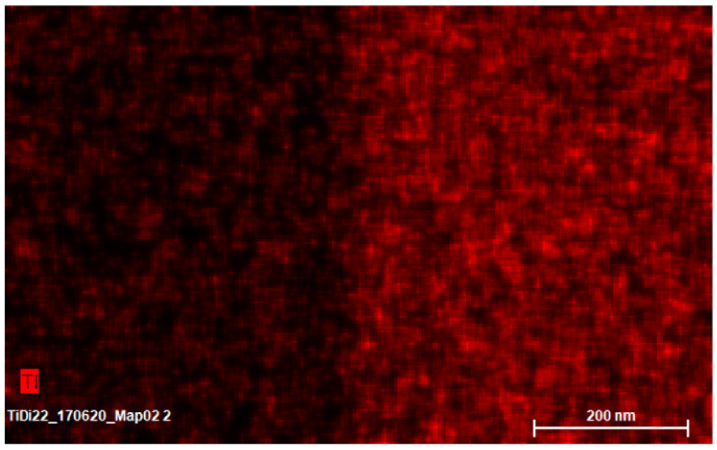

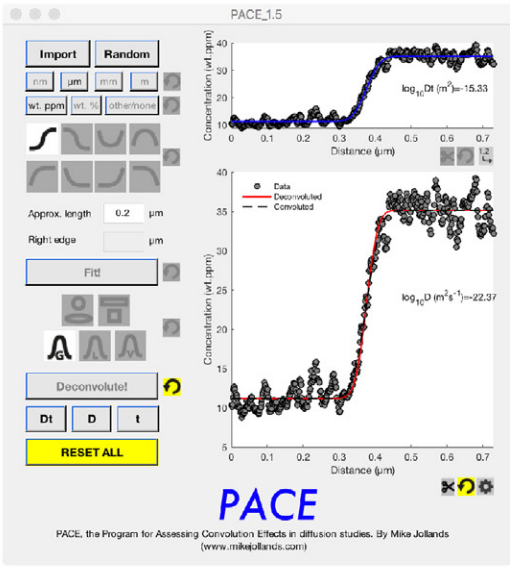

TiDi27 (= after annealing at 1400 °C, 0.3 GPa for 166 hrs)

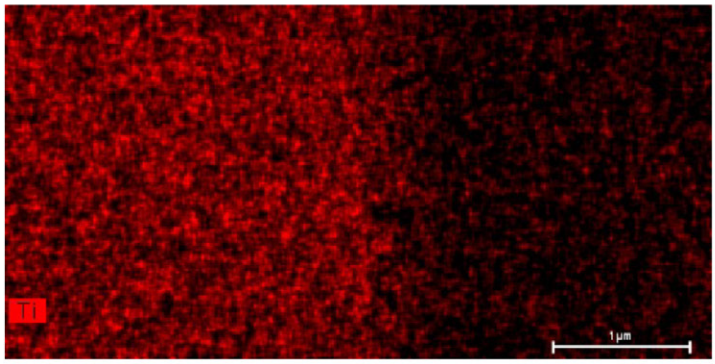

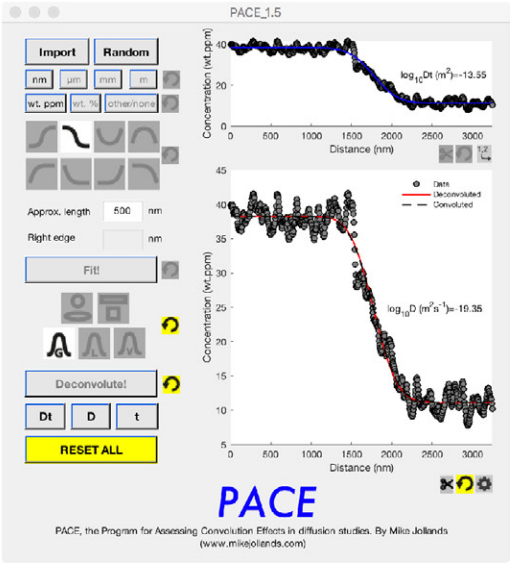

Supplementary Figure S9. Additional examples of quantitative Ti distribution maps obtained by TEM.

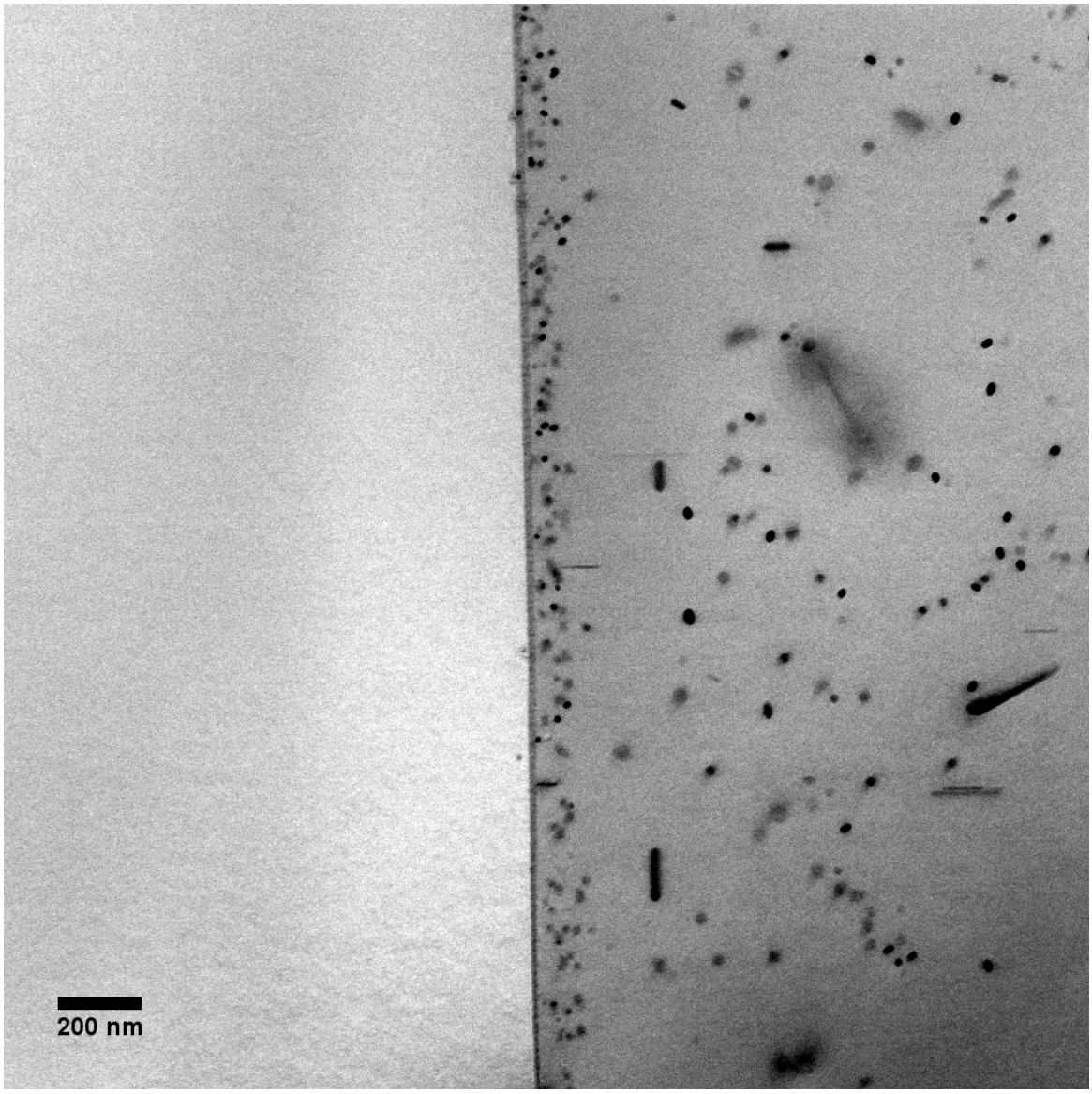

Supplementary Figure S10. Annular bright field image of the contact between Ti-poor quartz seed and Ti-rich quartz overgrowth in experiment TiDi17, which was performed with starting material SM02 at 1,000 °C, 1.5 GPa for 739 hrs. Due to the high pressure the TiO_2 solubility in the quartz was exceeded, resulting in exsolution of small rutile crystals (=black features) from the Ti-rich quartz.

Shaggy Peak sanidine phenocryst F2

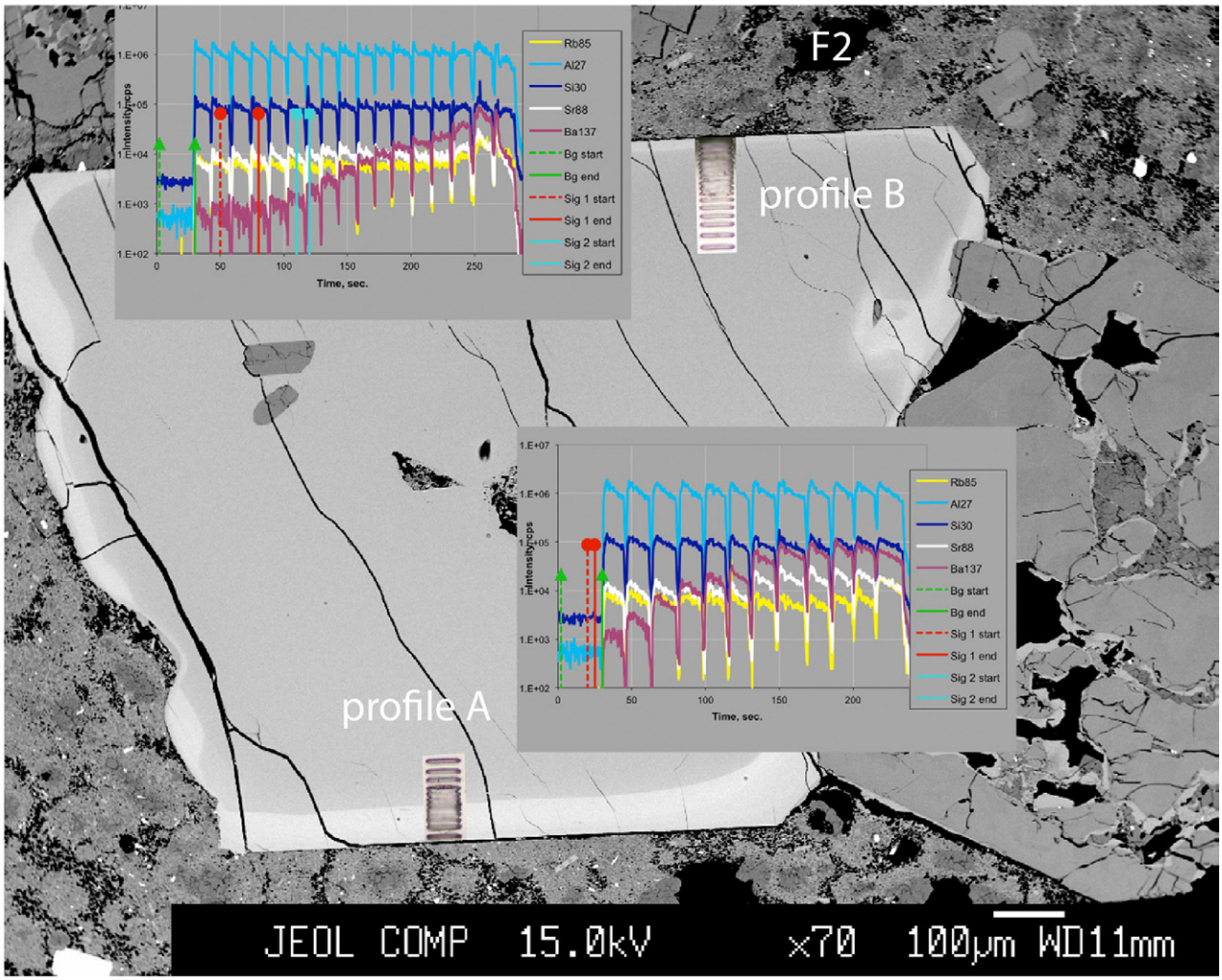

Fit of Ba in profile A

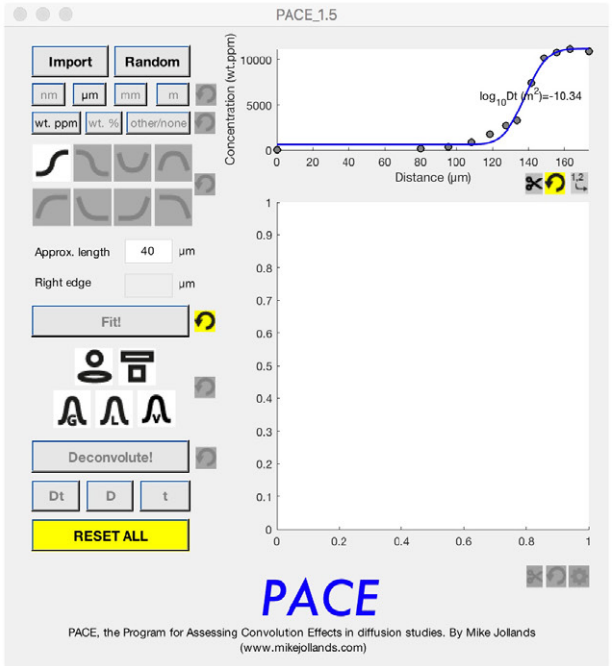

Fit of Ba in profile B

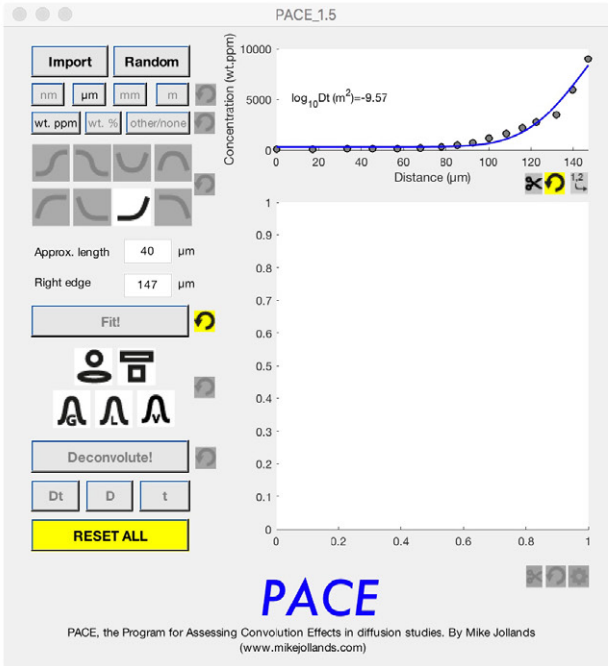

Supplementary Figure S11. BSE image of Shaggy Peak sanidine phenocryst F2, superimposed photomicrographs of LA-ICP-MS pits, LA-ICP-MS signals, and fits for Ba in the PACE program. Notice that the LA-ICP-MS signal is displayed on a logarithmic scale, which is why the Ba profile looks broader than on the BSE grayscale image.

Shaggy Peak sanidine phenocryst F3

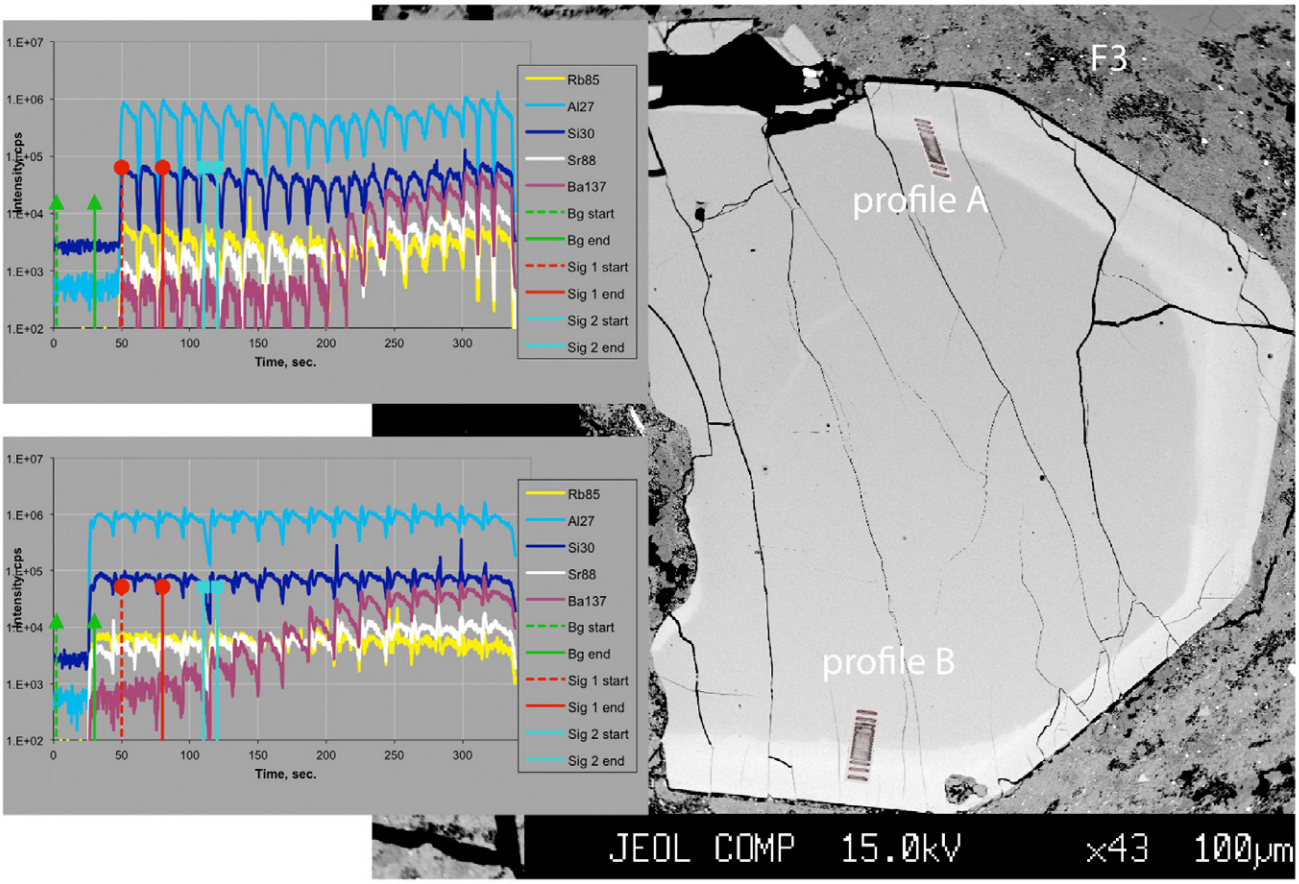

Fit of Ba in profile A

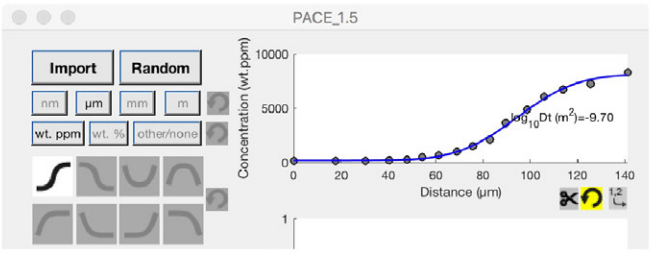

Fit of Sr in profile A

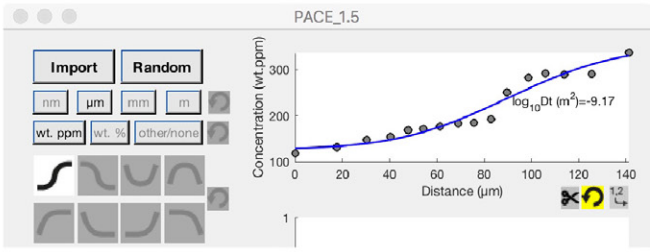

Fit of Ba in profile B

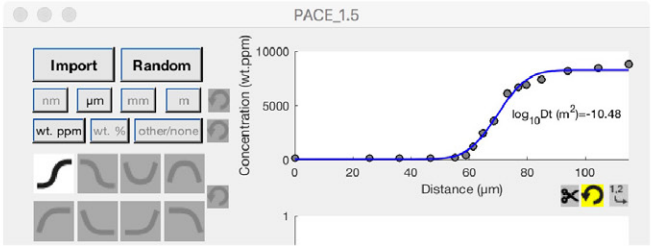

Fit of Sr in profile B

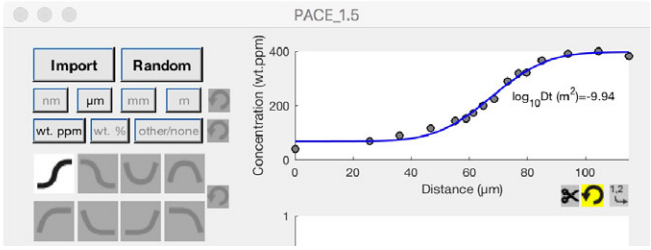

Supplementary Figure S12. BSE image of Shaggy Peak sanidine phenocryst F3, superimposed photomicrographs of LA-ICP-MS pits, LA-ICP-MS signals, and fits for Ba and Sr in the PACE program. Notice that the LA-ICP-MS signal is displayed on a logarithmic scale, which is why the Ba profile looks broader than on the BSE grayscale image.

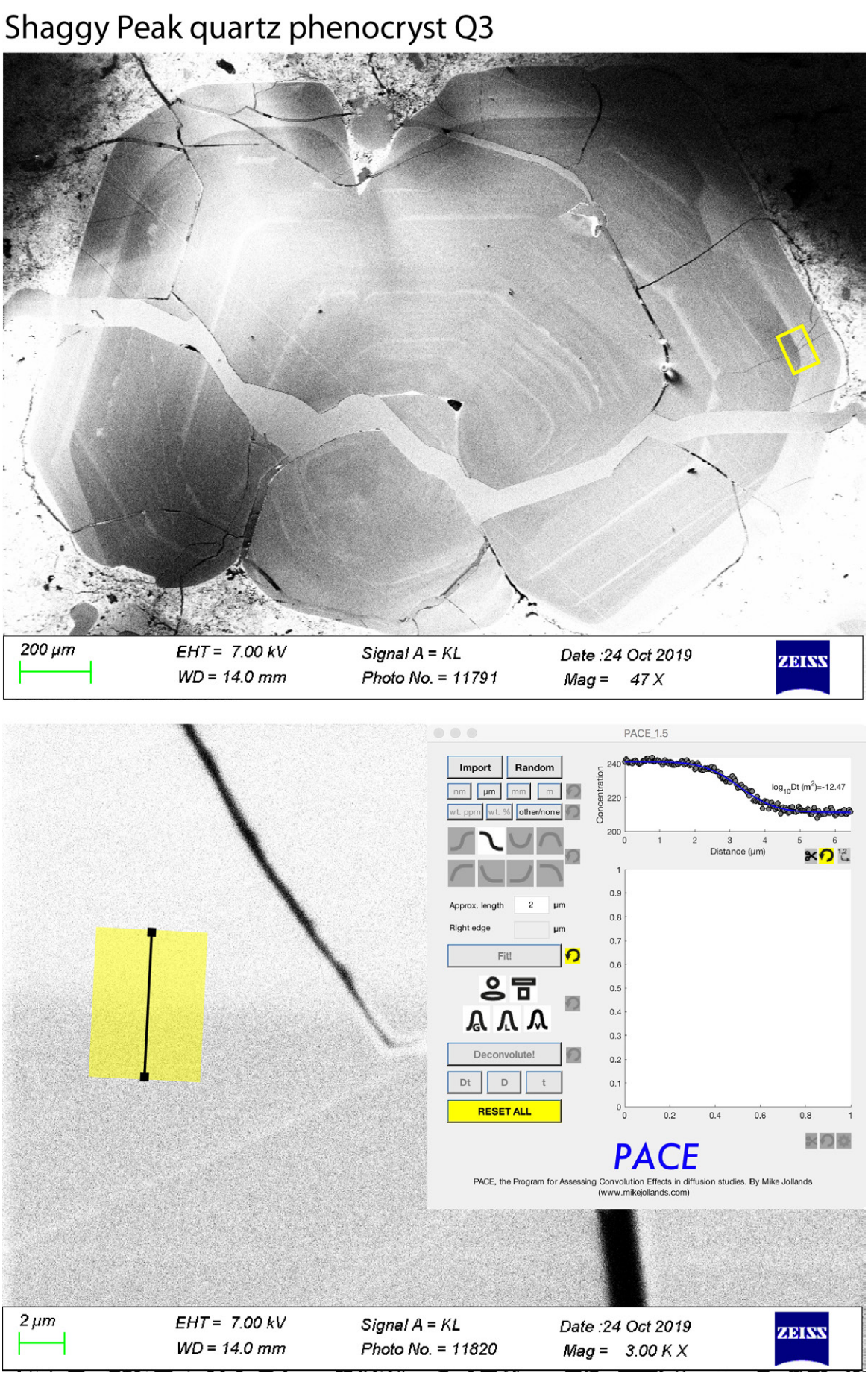

Supplementary Figure S13. CL image of Shaggy Peak quartz phenocryst Q3, the selected ImageJ profile (semitransparent, yellow area), and the corresponding PACE fit.

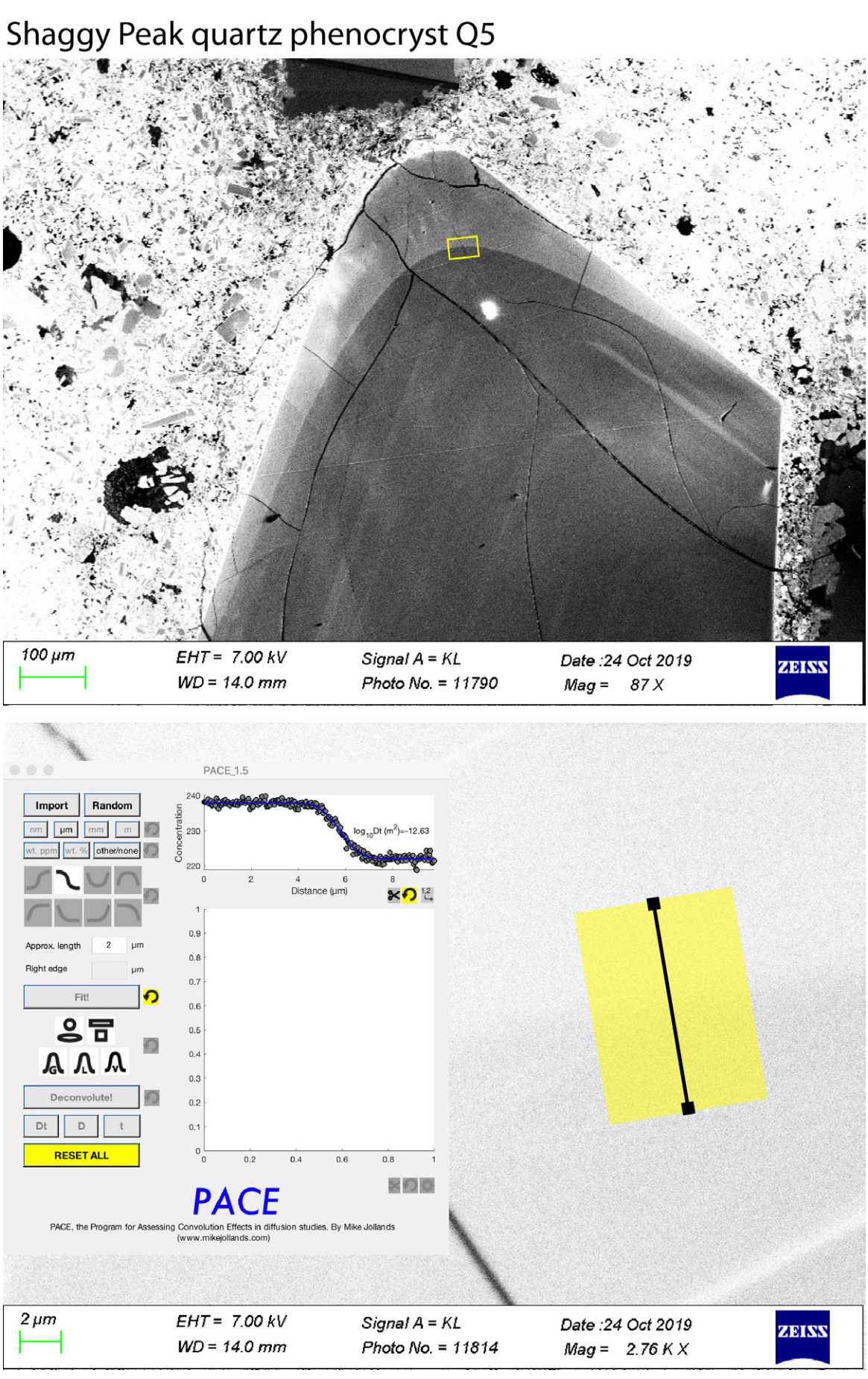

Supplementary Figure S14. CL image of Shaggy Peak quartz phenocryst Q5, the selected ImageJ profile (semitransparent, yellow area), and the corresponding PACE fit.

3. Supplementary Tables

Supplementary Table S1 Overview of experiments and obtained results

Run	Starting material[1]	T (°C)	P (GPa)	Duration (hrs)	FWHM based on CL (µm)	FWHM based on TEM (µm)	FWHM based on HIM-SIMS (µm)
Synthesis of diffusion couples							
SM01	qtz+rutile+glass+H_2O	1000	0.1	5	0.18	N/A	N/A
SM02	qtz+rutile+glass+H_2O	1000	0.1	4	0.19	0.041	0.069
SM03	qtz+rutile+H_2O	700	0.2	166	0.42 (fast scan)	N/A	N/A

Run	Starting material	T (°C)	P (GPa)	Duration (hrs)	log D based on CL (m^2/s)	convol.[2]	log D based on TEM (m^2/s)	convol.[2]	log D based on HIM-SIMS (m^2/s)	convol.[2]
Annealing experiments										
TiDi01	natural qtz phenocryst	1600	ca. 2.0	75	-17.36 ± 0.02	0.11	N/A		N/A	
TiDi08	SM01 (=high-Ti)	1600	ca. 2.0	74	-18.24 ± 0.01	0.01	N/A		N/A	
TiDi16	SM02 (=high-Ti)	1600	ca. 2.0	90	-18.52 ± 0.01	0.01	-19.09 ± 0.05	0.02	N/A	
TiDi06	SM01 (=high-Ti)	1600	ca. 2.0	90	-18.88 ± 0.01	0.10	N/A		-18.8 ± 0.2	0.01
TiDi46	SM03 (=low-Ti)	1100	0	891	<20.65 ± 0.13	N/A	N/A		N/A	
TiDi45	SM03 (=low-Ti)	1200	0	473	<20.26 ± 0.10	N/A	N/A		N/A	
TiDi47	SM03 (=low-Ti)	1300	0	73	<20.28 ± 0.15	N/A	N/A		N/A	
TiDi49	SM03 (=low-Ti)	1300	0	141	-20.26 ± 0.15	0.83	N/A		N/A	
TiDi40	SM03 (=low-Ti)	1100	2.0	811	-19.39 ± 0.29	0.06	N/A		N/A	
TiDi39	SM03 (=low-Ti)	1200	ca. 1.5	211	-19.24 ± 0.18	0.14	N/A		N/A	
TiDi44	SM03 (=low-Ti)	1200	ca. 1.3	424	-19.84 ± 0.29	0.23	N/A		N/A	
TiDi41	SM03 (=low-Ti)	1400	ca. 1.7	93	-18.18 ± 0.06	0.03	N/A		N/A	
TiDi42	SM03 (=low-Ti)	1500	ca. 1.7	67	-18.55 ± 0.14	0.09	N/A		N/A	
TiDi43	SM03 (=low-Ti)	1600	ca. 1.3	43	-19.06 ± 0.29	0.34	N/A		N/A	
TiDi22	SM02 (=high-Ti)	1000	0	2033	-22.14 ± 0.02	0.84	-22.37 ± 0.07	0.18	N/A	
TiDi23	SM02 (=high-Ti)	1100	0	812	-21.18 ± 0.03	0.42	-20.74 ± 0.06	0.01	N/A	
TiDi24	SM02 (=high-Ti)	1200	0	383	-21.22 ± 0.02	0.75	-20.55 ± 0.10	0.14	N/A	
TiDi27	SM02 (=high-Ti)	1400	ca. 0.3	166	N/A		-19.35 ± 0.05	0.02	N/A	

FWHM – Full width at half maximum; N/A – not applicable

[1] qtz – quartz; glass – SiO_2 glass

[2] logD subtracted during signal deconvolution

Supplementary Table S2 Diffusion data of Shaggy Peak Rhyolite

Mineral	Phenocryst	Profile	log Dt Ti (m^2)	log Dt Ba (m^2)	log Dt Sr (m^2)	Quality of fit[1]	Remarks[2]
quartz	Q1		-12.51	N/A		***	
quartz	Q3		-12.47	N/A		***	
quartz	Q5		-12.63	N/A		***	
quartz	Q7		-12.50	N/A		***	
sanidine	F2	A	N/A	-10.34	not fittable	** (Ba)	
sanidine	F2	B	N/A	-9.57	not fittable	* (Ba)	only half of the profile fitted
sanidine	F3	A	N/A	-9.70	ca. -9.17	** (Ba); * (Sr)	no plateaus for Sr
sanidine	F3	B	N/A	≤ -10.48	-9.94	** (Ba); ** (Sr)	small growth effect
sanidine	F6		N/A	-9.74	-8.57	* (Ba); *** (Sr)	
sanidine	F9	A	N/A	-10.99	ca. -8.97	*** (Ba); * (Sr)	no plateaus for Sr
sanidine	F9	B	N/A	-10.64	ca. -8.93	*** (Ba); * (Sr)	no plateaus for Sr

N/A – not applicable

[1] three stars means very good fit; one star means only partial fit

[2] growth effect means that part of the measured profile probably reflects an original growth zonination rather than a diffusion profile.

Supplementary Table S3 LA-ICP-MS analyses of melt inclusions and host quartz of the Shaggy Peak Rhyolite

Analysis	Sample	SiO_2 wt%	TiO_2 wt%	Al_2O_3 wt%	FeO_{tot} wt%	MnO wt%	MgO wt%	CaO wt%	Na_2O wt%	K_2O wt%	total wt%
20Oc26b09	Shag Q1 MI1 core 25µm	78.97	0.05	12.28	0.35	0.11	0.03	0.45	3.05	4.72	100.00
20Oc26b11	Shag Q1 MI2 rim17µm	78.46	0.09	12.50	0.50	0.05	0.23	0.75	2.92	4.50	100.00
20Oc26b13	Shag Q1 MI3 rim 17µm	79.11	0.08	12.44	0.49	0.05	0.13	0.75	2.72	4.23	100.00
20Oc26b17	Shag Q3 MI1 core 30µm	78.35	0.05	12.25	0.37	0.10	0.03	0.45	3.71	4.70	100.00
20Oc26c05	Shag Q3 MI2 rim 40µm	77.79	0.07	12.79	0.56	0.06	0.06	0.83	3.28	4.56	100.00
20Oc26c09	Shag Q10 MI1 core 35µm	78.76	0.05	12.40	0.37	0.11	0.03	0.44	3.38	4.46	100.00
20Oc26c10	Shag Q10 exposed MI core 40µm	77.93	0.05	12.51	0.39	0.11	0.04	0.31	3.90	4.77	100.00
20Oc26c11	Shag Q6 exposed MIcore 40µm	77.92	0.05	12.31	0.39	0.10	0.04	0.44	3.95	4.80	100.00

Supplementary Table S3 (contd.)

Analysis	Sample	B µg/g	Rb µg/g	Sr µg/g	Y µg/g	Zr µg/g	Nb µg/g	Mo µg/g	Sn µg/g	Cs µg/g	Ba µg/g
20Oc26b09	Shag Q1 MI1 core 25µm	85	313	5	39	42	41	2	(8)	16	8
20Oc26b11	Shag Q1 MI2 rim17µm	(31)	160	84	20	72	15	2	(18)	5	527
20Oc26b13	Shag Q1 MI3 rim 17µm	(40)	149	80	16	62	18	(2)	(23)	4	460
20Oc26b17	Shag Q3 MI1 core 30µm	83	292	14	40	43	42	1	(11)	16	34
20Oc26c05	Shag Q3 MI2 rim 40µm	38	179	90	20	68	20	2	(3)	6	606
20Oc26c09	Shag Q10 MI1 core 35µm	65	309	3	38	45	41	1	(3)	15	4
20Oc26c10	Shag Q10 exposed MI core 40µm	69	335	3	35	45	41	2	(4)	18	7
20Oc26c11	Shag Q6 exposed MIcore 40µm	88	327	2	33	47	41	1	3	17	1

Supplementary Table S3 (contd.)

Analysis	Sample	Ce µg/g	W µg/g	Pb µg/g	Bi µg/g	U µg/g	Th µg/g	Ti qtz µg/g	FM	T zirc[1] °C	$aTiO_2$[2]	P TitaniQ[3] MPa
20Oc26b09	Shag Q1 MI1 core 25µm	26	4	50	1	21	17	32	1.26	699	0.75	435
20Oc26b11	Shag Q1 MI2 rim17µm	41	(3)	43	(1)	6	21	52	1.34	739	0.75	384
20Oc26b13	Shag Q1 MI3 rim 17µm	40	(4)	34	(1)	6	19	52	1.23	733	0.74	353
20Oc26b17	Shag Q3 MI1 core 30µm	26	4	43	1	19	16	35	1.40	692	0.66	321
20Oc26c05	Shag Q3 MI2 rim 40µm	41	3	45	0	8	22	53	1.37	730	0.71	322
20Oc26c09	Shag Q10 MI1 core 35µm	28	4	48	1	18	19	35	1.28	703	0.72	394
20Oc26c10	Shag Q10 exposed MI core 40µm	26	4	52	1	18	16	35	1.40	695	0.68	344
20Oc26c11	Shag Q6 exposed MIcore 40µm	28	4	58	1	17	21	n.a.	1.47	694	0.69	N/A

n.a. – not analyzed; N/A – not applicable; red numbers in parentheses denote dectection limits
[1] zircon saturation temperature according to Watson and Harrison (1983) assuming 68.2 wt% ZrO_2 in zircon
[2] activity of TiO_2 in the silicate melt according to the TiO_2 solubility model of Kularatne and Audétat (2014)
[3] TitaniQ pressure according to the model of Huang and Audétat (2012)

4. Supplementary References

Audétat, A., 2013, Origin of Ti-rich rims in quartz phenocrysts from the Upper Bandelier Tuff and the Tunnel Spring Tuff, southwestern USA: Chemical Geology, v. 360-361, p. 99-104.

Dowsett, D., and Wirtz, T., 2017, Co-registered in situ secondary electron and mass spectral imaging on the Helium Ion Microscope demonstrated using lithium titanate and magnesium oxide nanoparticles: Analytical Chemistry, v. 89, p. 8957–8965.

Ginibre, C., Wörner, G., and Kronz, A., 2004, Structure and dynamics of the Laacher See magma chamber (Eifel, Germany) from major and trace element zoning in sanidine: a cathodoluminescence and electron microprobe study: Journal of Petrology, v. 45, p. 2197-2223.

Kim, S., Trofimov, A., Khanom, F., Stern, L., Lamberti, W., Colby, R., Abmayr, D., Belianinov, A., and Ovchinnikova, O.S., 2019, High-resolution multimodal

chemical imaging platform for organics and inorganics: Analytical Chemistry, v. 91, p. 12142–12148.

Kularatne, K., and Audétat, A., 2014, Rutile solubility in hydrous rhyolite melts at 750-900 °C and 2 kbar, with application to titanium-in-quartz (TitaniQ) thermobarometry: Geochimica et Cosmochimica Acta, v. 125, p. 196-209.

Thomas, J. B., Watson, E. B., Spear, F. S., Shemella, P. T., Nayak, S. K., and Lanzirotti, A., 2010, TitaniQ under pressure: the effect of pressure and temperature on the solubility of Ti in quartz: Contributions to Mineralogy and Petrology, v. 160, p. 743-759.

Usiobo, O.J., Kanda, H., Gratia, P., Zimmermann, I., Wirtz, T., Nazeeruddin, M.K., and Audinot, J.-N., 2020, Nanoscale mass-spectrometry imaging of grain boundaries in perovskite semiconductors: The Journal of Physical Chemistry C, doi:10.1021/acs.jpcc.0c07464.

Watson, B. E., and Harrison, M. T., 1983, Zircon saturation revisited: temperature and composition effects in a variety of crystal magma types: Earth and Planetary Science Letters, v. 64, p. 295-304.